Kinetics and Product Branching Ratios of the Reaction of $^1CH_2$ with H_2 and D_2†

K. L. Gannon, M. A. Blitz, M. J. Pilling, and P. W. Seakins*

School of Chemistry, University of Leeds, Leeds, LS2 9JT, United Kingdom

S. J. Klippenstein* and L. B. Harding

Chemical Sciences and Engineering Division, Argonne National Laboratory, Argonne, Illinois 60439

Received: April 8, 2008; Revised Manuscript Received: June 26, 2008

The reactions of singlet methylene (a^1A_1 $^1CH_2$) with hydrogen and deuterium have been studied by experimental and theoretical techniques. The rate coefficients for the removal of singlet methylene with H_2 (k_1) and D_2 (k_2) have been measured from 195 to 798 K and are essentially temperature-independent with values of $k_1 = (10.48 \pm 0.32) \times 10^{-11}$ cm^3 molecule^{-1} s^{-1} and $k_2 = (5.98 \pm 0.34) \times 10^{-11}$ cm^3 molecule^{-1} s^{-1}, where the errors represent 2σ, giving a ratio of $k_1/k_2 = 1.75 \pm 0.11$. In the reaction with H_2, singlet methylene can be removed by reaction giving $CH_3 + H$ or deactivated to ground-state triplet methylene. Direct measurement of the H atom product showed that the fraction of relaxation decreased from 0.3 at 195 K to essentially zero at 398 K. For the reaction with deuterium, either H or D may be eliminated. Experimentally, the H:D ratio was determined to be 1.8 ± 0.5 over the range 195−398 K. Theoretically, the reaction kinetics has been predicted with variable reaction coordinate transition state theory and with rigid-body trajectory simulations employing various high-level, ab initio-determined potential energy surfaces. The magnitudes of the calculated rate coefficients are in agreement with experiment, but the calculations show a significant negative temperature dependence that is not observed in the experimental results. The calculated and experimental H to D ratios from the reaction of singlet methylene with D_2 are in good agreement, suggesting that the reaction proceeds entirely through the formation of a long-lived methane intermediate with a statistical distribution of energy.

1. Introduction

Singlet methylene, a^1A_1, the first excited state of methylene (hereafter referred to as $^1CH_2$), is an important intermediate in combustion[1,2] and planetary atmospheres.[3−6] For example, the reaction of singlet methylene with acetylene forming the propargyl radical is an important route to soot formation.[7−9] The removal of singlet methylene can occur via reaction, deactivation, or a combination of the two processes. For rare and inert gases, only the deactivation can occur, and this is thought to occur via a gateway mechanism[10] with a positive temperature dependence. For molecular species, there is a competition between reaction and relaxation. Rate coefficients for reaction of $^1CH_2$ generally have a weak or negative temperature dependence. If relaxation occurs via the same mechanism as for the rare gases, with a positive temperature dependence, then one would expect relaxation to dominate at combustion temperatures and reaction to dominate under conditions relevant for outer planetary atmospheres or interstellar chemistry.

The competition between reaction and deactivation is of potential significance as, despite the relatively small difference in heats of formation ($\Delta E_{298} = 9.01$ kcal mol^{-1} [11]) of the ground-state triplet (X^3B_1, represented as $^3CH_2$) and the singlet state, singlet methylene is several orders of magnitude more reactive at room temperature. $^1CH_2$ reactions tend to occur via insertion mechanisms with zero or negative activation energies[12] in contrast to reactions of the triplet ground state, which generally have significant and positive activation energies.

The reaction of $^1CH_2$ with H_2 is an important loss process for $^1CH_2$ in both combustion and planetary atmospheres; the following processes can take place

$$^1CH_2 + H_2 \xrightarrow{k_{1a}} {}^3CH_2 + H_2$$

$$\xrightarrow{k_{1b}} CH_3 + H$$

The reactive channel (1b) proceeds via an insertion reaction to give a methane intermediate that dissociates to methyl + H. At very high pressure, significantly higher than those used in this and previous studies, stabilization of methane could compete with dissociation. For the corresponding reaction of $^1CH_2$ with D_2, either H or D atoms can be formed from the break up of the CH_2D_2 intermediate:

$$^1CH_2 + D_2 \xrightarrow{k_{2a}} {}^3CH_2 + D_2$$

$$\xrightarrow{k_{2b}} CHD_2 + H$$

$$\xrightarrow{k_{2c}} CH_2D + D$$

The kinetics of the removal of $^1CH_2$ with H_2 have been studied previously,[13−17] most comprehensively by Hancock and co-workers.[16,17] Early measurements of k_1 were limited to room temperature ($k_1 = 1.05 \times 10^{-10}$ [14] and 1.30×10^{-10} cm^3 molecule^{-1} s^{-1} [13]), but subsequently, kinetic measurements were

† Part of the "Stephen R. Leone Festschrift".

10.1021/jp803038s CCC: $40.75
Published on Web 08/20/2008

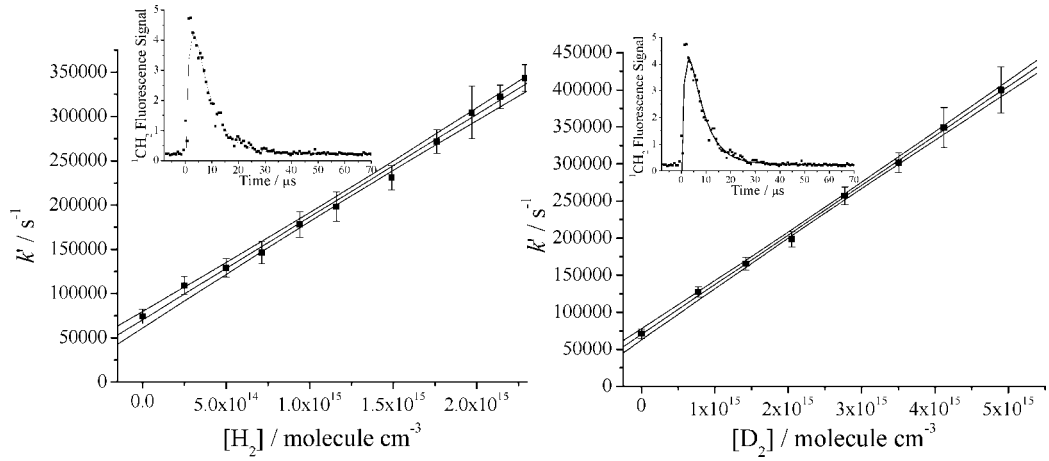

Figure 1. Typical bimolecular plots for $^1CH_2 + H_2/D_2$ at 298 K probing the $^PR_{1,J-1}$ branch $J = 3$ (ortho 3_{12}) with typical pseudo first-order $^1CH_2$ decay plots in the inset. The error bars represent the statistical (2σ) uncertainty in the experimental results.

performed from room temperature up to 431[16] and 676 K.[17] In both cases, a slight negative temperature dependence in the overall kinetics was observed with k_1 decreasing from ~1.0 to ~0.8×10^{-10} cm^3 molecule^{-1} s^{-1}. The reaction has also been studied as a function of temperature (210−475 K) by Wagener,[15] who reported a slightly stronger negative temperature dependence with k_1 decreasing from 1.35 to 0.93×10^{-10} cm^3 molecule^{-1} s^{-1}.

There have been limited studies at low temperature. Capture theory for a dispersion potential[18] suggests that the low temperature rate coefficient should be $3.6 \times 10^{-10}\ T^{1/6}$ cm^3 molecule^{-1} s^{-1}, where T is in K. At 300 K, this correlates with a rate coefficient of 9×10^{-10} cm^3 molecule^{-1} s^{-1}, which is an order of magnitude greater than the observed room temperature values near 1×10^{-10} cm^3 molecule^{-1} s^{-1}. The low value observed experimentally implies that short-range forces are already important at room temperature. At some point, one expects to see a substantial increase in the rate coefficient with decreasing temperature as the transition state moves out to large separations and the rate coefficient approaches the capture theory value.

In the present study, the rate of removal of $^1CH_2$ with H_2 and D_2 has been studied experimentally over a wide range of temperatures. As far as we are aware, this is the first reported study of the kinetics of $^1CH_2$ with D_2. We also provide a detailed theoretical study of the temperature dependence for the reactive channel. This theoretical analysis includes predictions of the branching between the H and the D loss channels for the reaction with D_2.

Previous studies in this laboratory[19] have shown that for this system the reactive branching ratio increases with temperature from 0.85 at room temperature to essentially 100% reaction by 500 K. This room temperature measurement is essentially consistent with an earlier study by Braun et al.[20] who reported a reactive branching ratio of 0.80.

In this study, we explore how the branching ratio changes at lower temperature and examine the H and D absolute and relative yields from the reaction of $^1CH_2$ with D_2 to determine information on the life of the CH_2D_2* intermediate. Both the kinetics and the product yields of these reactions have been examined experimentally and theoretically, building on the approach exemplified in a recent series of articles.[21] While qualitative agreement on the kinetics and branching ratios of the reaction is obtained, significant differences exist between theory and experiment, and these are explored in the discussion.

2. Experimental Section

The experimental studies were carried out in a slow-flow apparatus using laser flash photolysis of ketene to generate $^1CH_2$ and probing the concentration of $^1CH_2$ reactant and H or D product via laser-induced fluorescence (LIF) in the presence of excess H_2 or D_2 reagent. The apparatus was described in previous publications.[22−24] The reaction cell was a six-way stainless steel cross that could be either heated (via cartridge heaters located in the main body of the reactor) or cooled by immersion into a bath of dry ice/acetone. The temperature was monitored by thermocouples placed just above and below the reaction zone. The $^1CH_2$ precursor, ketene, substrate (H_2, BOC 99.999%, or D_2 Air Products, 99.999%, used without further purification), in excess, and He bath gas were flowed through calibrated mass flow controllers and mixed before introduction into the cell. The total flow rate was sufficient that a fresh flow of gas was photolyzed by each laser pulse and the total pressure (as measured by a 0−10 Torr baratron) was controlled by a throttle valve on the exit line to the pump. The reaction cell was maintained at pressures below 10^{-4} Torr overnight.

Ketene was generated by the pyrolysis of acetic anhydride[25] and purified by trap-to-trap distillation, and the purity was checked by IR spectroscopy.[26] $^1CH_2$ was generated by pulsed photolysis of ketene at 308 nm using an excimer laser (Questek vβ 2000, 10 Hz, 60 mJ per pulse):

$$CH_2CO + h\nu \rightarrow {}^1CH_2 + CO$$

At these laser intensities, ketene photolysis is a clean source of methylene, and at this wavelength, the fractional yield of $^3CH_2$ is less than 5%.[27,28]

For the kinetics experiments, the time-dependent concentration of $^1CH_2$ was probed using pulsed LIF, exciting the $b^1B_1 \leftarrow a^1A_1$ transition at ~589.25 nm using light from an excimer pumped dye laser (Lambda Physik LPX 100 pumping a Lambda Physik FL3002 with Rhodamine 6G) introduced perpendicularly to the photolysis laser pulse. Fluorescence was collected through a Perspex filter by a photomultiplier mounted perpendicularly to both laser beams and interfaced to a boxcar averager. The time between the photolysis and the probe laser pulses was varied to build up the temporal profile of the $^1CH_2$, and a typical example is shown in the inset to Figure 1. The profile is biexponential in nature with a fast rise due to rotational relaxation of the photolytically produced $^1CH_2$. This relaxation is fast as compared to the reaction with the substrate. Under

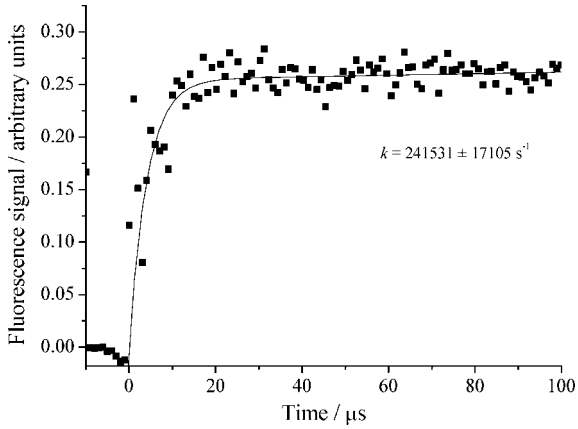

Figure 2. Typical first-order H atom growth trace, where the black data points are the raw signals and the solid line through the data is the biexponential fit to the data giving a pseudo first-order rate coefficient of 242000 ± 17000 s^{-1}. The comparable pseudo first-order loss of $^1CH_2$ is 230000 ± 19000 s^{-1}.

the experimental conditions where $[H_2]$ or $[D_2]$ was very much greater than $[^1CH_2]$, then $^1CH_2$ is removed by pseudo first-order kinetics and

$$k' = k_{bi}[H_2] + k_{loss}$$

where k_{bi} is the bimolecular rate coefficient to be determined and k_{loss} is the total rate coefficient for the other minor first-order loss processes (diffusion and relaxation via the buffer gas). A plot of k' vs $[H_2]$ gives a straight line of gradient k_{bi} and intercept k_{loss}. Figure 1 shows examples of such linear plots, and the small intercept demonstrates that reaction with the substrate dominates $^1CH_2$ removal. The experiments were repeated at a range of temperatures between 195 and 795 K with both H_2 and D_2 substrates.

For product studies, the H or D atom signal was monitored by LIF at the Lyman α transition (~121.6 nm). Lyman α radiation was generated by frequency tripling the output of an excimer pumped dye laser at ~365.8 nm in a krypton/argon mix (~800 Torr). A krypton to argon ratio of 1:2.5 was optimal for the H atom studies. For experiments requiring rapid scanning between H and D atom signals, the mix was adjusted to 1:2.3 to give approximately equal outputs at wavelengths for H and D excitation. As for the earlier studies, fluorescence was collected perpendicularly to the photolysis and probe lasers using a solar blind PMT (Thorn EMI). The probe laser intensity was measured with a second PMT mounted equidistant from the reaction zone, and the output from this PMT was used to normalize the fluorescence signal on a shot-to-shot basis and to account for the absorption of Lyman α radiation by the substrate gases. Some kinetic traces, an example of which is shown in Figure 2, were carried out to confirm that H atoms were produced with the same pseudo first-order rate coefficient with which $^1CH_2$ was removed. Within experimental error, the measured pseudo first-order rate coefficient agreed with the calculated pseudo first-order rate coefficient determined from the earlier kinetic studies, confirming that H atoms are produced from the target reaction and not from any minor photolysis coproducts or secondary chemistry.

2.1. Calibration of H and D Atom Signals. LIF is a relative technique; hence, the H atom signal needs to be calibrated for yield measurements. For $^1CH_2 + H_2$, the methodology for this process has been described in a previous publication,[19] and absolute branching ratios for H atom production are known at room temperature and above. This reaction can therefore be used as a calibration reaction for the H atom yield from $^1CH_2 + D_2$. For temperatures below room temperature, new calibrations were required.

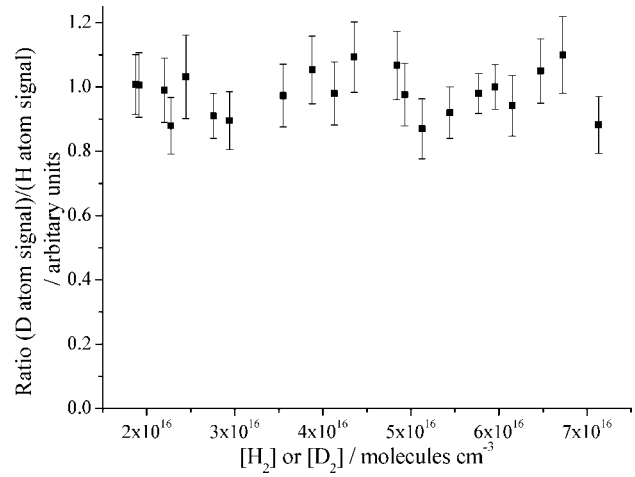

Figure 3. Comparison of H and D atom signals generated from the reaction of $O^1D + H_2$ and D_2, respectively. The H atom signal for each given $[H_2]$ was compared to the corresponding D atom signal for the same $[D_2]$ under identical experimental conditions. The $[N_2O]$ remained constant at 3.5×10^{14} molecules cm^{-3}. The reported errors represent statistical uncertainty (2σ) in the experimental data.

Our earlier calibration was based on an end product study by Temps and co-workers who determined the absolute H atom yield from the $^3CH_2 + NO$ reaction at room temperature and above.[29] By carrying out the reaction in a high concentration of helium, all of the $^1CH_2$ can be deactivated to $^3CH_2$; thus, the H atom signal can be correlated with the initial $^1CH_2$ concentration. However, the H atom yield from the $^3CH_2 + NO$ reaction has not been measured below room temperature. Previous work in this laboratory[24] has shown that $^1CH_2$ is rapidly deactivated by O_2. $^3CH_2$ then reacts with O_2 with an H atom yield of (0.83 ± 0.14), which is temperature-independent over the range of 298−598 K. This value has been used to normalize the H atom signal at 195 K, assuming that the H atom yield remains invariant.

To interpret the relative H and D atom signals, the detection efficiencies for the two atoms must be determined. While the absorption cross-sections and fluorescence yields will be virtually identical, the laser power at the two wavelengths may not be identical and the line width of the H atom line will be significantly greater than that of the D atom.

To calibrate the system, identical concentrations of $O(^1D)$ were generated in the presence of excess H_2 and D_2 in repeated back-to-back experiments from the photolysis of N_2O at 193 nm (GAM laser Inc. model EX5, 8 mJ $pulse^{-1}$). Such experiments should generate identical short time concentrations of H and D via the reactions

$$O(^1D) + H_2 \rightarrow OH + H$$

and

$$O(^1D) + D_2 \rightarrow OD + D$$

The signals of H and D are shown in Figure 3 and demonstrate that the detection efficiency for both atoms is the same at 298 K. This is consistent with an experimental measurement of the line width of the H atom spectrum, which gives a tripled laser line width of 0.6 cm^{-1}, larger than the Doppler line width of H (0.5 cm^{-1}) and hence appreciably larger than the line width of the heavier D atom. In both cases, the laser line should "sit

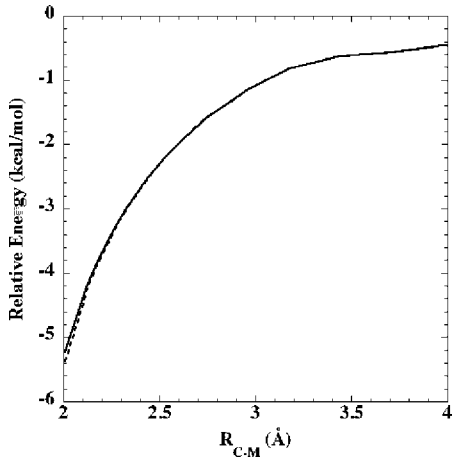

Figure 4. Plot of the optimized CCSD(T)/aug-cc-pvdz $^1CH_2\cdots H_2$ interaction energy as a function of the distance R_{CM} between the C atom and the center of mass of H_2. The dashed line denotes the fully optimized results, while the solid line denotes results for the $^1CH_2$ and H_2 geometries fixed in their infinite separation equilibrium geometries.

over" the Doppler width of the atom. At the highest temperature of the yield experiments, 398 K, the Doppler width will be increased by ~15% over the 298 K value; therefore, an additional 10% error has been factored into the yield ratios at this temperature to allow for the possibilities of slight variations in H and D atom detection efficiencies. In the yield experiments for $^1CH_2 + D_2$, the H and D atom signals were put on an absolute scale from our previous measurements on $^1CH_2$ with H_2.[19]

3. Theoretical Calculations

The present theoretical analysis focuses on the kinetics and branching of the reactive channels in the reaction of $^1CH_2$ with H_2 and D_2. We consider both the high-pressure limit for the addition/insertion to form CH_4 and the low-pressure limit for the branching between H and D from the CH_2D_2 complex. Sample master equation simulations indicate that, for the pressure range of interest here, there is no stabilization of the CH_4 complex and that the flux back toward reactant is negligible. Thus, the low-pressure limit is applicable to the branching and the high-pressure limit is appropriate for the total reaction rate coefficient. The prediction of the collisional relaxation to $^3CH_2$ is considerably more complicated and is deemed beyond the scope of the present theoretical analysis. The present predictions for the reactive channels should provide a lower bound to the observed total rate coefficient for loss of $^1CH_2$.

Early quantum chemistry studies indicated that the reaction of $^1CH_2$ with H_2 proceeds along a barrierless insertion path to the formation of methane, CH_4.[12,30] Subsequent analyses employing larger basis sets and improved correlation treatments verified the barrierless nature of the reaction.[31,32] The present analysis further confirms this conclusion as illustrated in Figure 4, where the results of constrained optimizations performed at the CCSD(T)/aug-cc-pvdz level are plotted.

The direct variable reaction coordinate transition state theory (VRC-TST) approach provides a useful approach for predicting the kinetics of such barrierless reactions.[33,34] This approach couples direct ab initio quantum chemical evaluations of the interaction energies with a phase space integral-based representation of transition state theory to provide an accurate treatment of the highly coupled anharmonic orientational modes of the transition state. An early application of this methodology to the closely related dissociation of ketene, CH_2CO, into $^1CH_2 + CO$ yielded good agreement with experimental observations.[35]

Here, we implement the VRC-TST approach for both the $^1CH_2 + H_2$ and the $^1CH_2 + D_2$ entrance channels, as well as for the $CH_2D + H$ and $CHD_2 + H$ exit channels. For the exit channel calculations, we employ a Davidson corrected[36,37] multireference configuration interaction (CAS + 1 + 2 + QC) analytic potential surface as described earlier.[38] A two-electron two-orbital reference space consisting of the CH_3 and H radical orbitals was employed for the reference space in these CAS + 1 + 2 + QC calculations. Dunning's augmented correlation consistent polarized valence quadruple-ζ basis was employed for these evaluations.[39,40]

For the entrance channel calculations, coupled cluster methods such as CCSD(T)[41] or QCISD(T)[42] are applicable since the reactants are not radicals. While such coupled cluster calculations should be highly accurate and are feasible for the present reaction, they are relatively time-consuming. One side goal of this work was to devise a scheme that would also be appropriate for treating the reactions of $^1CH_2$ with other hydrocarbons, particularly unsaturated hydrocarbons such as alkenes and alkynes. Such reactions are important in the hydrocarbon growth processes occurring during combustion and pyrolysis. For example, the reaction of $^1CH_2$ with acetylene is a dominant pathway to propargyl, whose self-recombination is generally regarded as the key step in the formation of the first aromatic.

For this reason, we have also explored the applicability of CASPT2 methods[43,44] for the entrance channel. Preliminary comparisons found that CASPT2 calculations employing state averaged wave functions were in better agreement with both QCISD(T) and CAS + 1 + 2 + QC calculations than were CASPT2 calculations employing non-state-averaged wave functions. This improved performance for the state-averaged wave function may be related to the difficulty of treating nearly degenerate states with CASPT2. For a two-electron two-orbital active space comprised of the orbitals correlating with the highest occupied and lowest unoccupied molecular orbitals of $^1CH_2$, the QCISD(T) and CAS + 1 + 2 + QC sample rate predictions differ by less than 10%, with the CASPT2 calculations falling more or less midway between the two. For the final calculations, we chose to employ the state-averaged two-electron two-orbital CASPT2 method, since it allowed for the most efficient consideration of large basis sets and large sets of dividing surfaces.

The entrance channel calculations were performed for a variety of basis sets (cc-pvdz, cc-pvtz, aug-cc-pvdz, and aug-cc-pvtz) including two separate extrapolations to the CBS limit.[45] CBS1 results are based on extrapolations of the cc-pvdz and cc-pvtz results, while CBS2 results are based on extrapolations of the aug-cc-pvdz and aug-cc-pvtz results. For temperatures above 100 K, the CBS1 and CBS2 extrapolations yield corrections relative to the cc-pvtz and aug-cc-pvtz results for the high-pressure addition rate constant of 25% or less and 5% or less, respectively. The final CBS1 and CBS2 extrapolated results are within 18% of each other. The theoretical predictions reported below are the average of the CBS1 and CBS2 results.

The variations in the conserved vibrational modes of $^1CH_2$ and H_2 along the reaction path, such as geometrical relaxation of the structures and changes in the vibrational frequencies, can have a significant effect on the rate coefficient. However, the plot of the energies along a distinguished reaction coordinate path (cf. Figure 4) indicates that, for the present reaction, the effects of geometry relaxation are insignificant. For example, a separation of 2.0 Å between the C atom and the center of mass

of H_2 correlates with the optimal canonical dividing surface at 1200 K. At this separation, the optimized interaction energy for CH_2 and H_2 constrained to their free fragment geometries is -5.2 kcal mol^{-1}. Meanwhile, the geometrical relaxation energy is less than 0.2 kcal mol^{-1}, which implies a change of only a few % in the predicted rate coefficient. At larger separations, the geometrical relaxation energy decreases in both an absolute and a relative sense. Similarly small effects are expected for variations in the conserved mode frequencies. Thus, the effects of conserved mode variations are not considered further here.

The Monte Carlo integrations involved in the VRC-TST evaluations were converged to 5% or better. Various sets of pivot points were considered, including ones located at the center of mass to treat the transition state at large separations and ones displaced perpendicularly from the CH_2 plane along the empty p-orbital. The VRC-TST calculations were performed at the energy E and total angular momentum J resolved level. This treatment allows for the proper conservation of angular momentum between collisions for both the collisionless limit bimolecular rate coefficients and the high-pressure insertion rate coefficients.

Previous comparisons of variable reaction coordinate transition state theory predictions with trajectory simulations suggest that VRC-TST slightly overestimates the rate constant.[33,34] In particular, for a series of R + H reactions, the trajectory rate coefficients were generally found to be about 0.9 times the VRC-TST predictions. Similarly, for the $CH_3 + CH_3$ reaction, a dynamical correction factor of 0.85 was typical. The present reaction may be somewhat different dynamically, particularly since the two reactants are not simple radicals. Thus, the dynamical correction factor may deviate somewhat from these prior values. Notably, a smaller value for the dynamical correction factor would help rationalize some of the deviation between theory and experiment seen below. Thus, we have chosen to perform rigid body trajectory simulations for the $^1CH_2 + H_2$ insertion reaction as well.

To this end, we fit an analytic, five-dimensional surface for the interaction between a rigid $^1CH_2$ and a rigid H_2. The calculations used in this fit were done at the CCSD(T)/aug-cc-pvtz level. Approximately 11000 points were calculated. Inclusion of permutation symmetry expands this list to ~35000 points. The points were fit to a sequence of five, fourth-order, six-dimensional, direct product, multinomials in Morse variables[46] with overlapping ranges for the $^1CH_2$ to H_2 distance. Note that although the final surface is of dimension five, six internuclear distances are allowed to vary; hence, the multinomials are functions of these six variables. The five individual fits are connected by switching functions to yield the final analytic potential used in the trajectory calculations. For the ~8000 points within ±5 kcal mol^{-1} of the $^1CH_2 + H_2$ asymptote, the fit yields an rms error of <0.5 kcal mol^{-1}. To further test the reliability of the fit, the TST calculations were repeated using the analytic surface and found to be in excellent agreement with the TST calculations done using ab initio points directly. Furthermore, this CCSD(T)/aug-cc-pvtz surface yields rate coefficients that are in reasonable agreement (~10−20%) with the CASPT2/CBS-based ones.

The microcanonical reactive flux, $N(E,R)$, is plotted in Figure 5 as a function of the dividing surface for a range of energies. These plots show some modest signs of the two transition state behavior that was central to the modeling of the related CH_2CO dissociation.[35] In particular, at low energies, there are clear minima in the flux plots at large R (e.g., $R = 10-14$ Bohr). At higher energies, there are instead inner minima for short R (e.g., $R = 4-6$ Bohr). At intermediate energies (e.g., $E = 0.324$ kcal mol^{-1}), there are slight maxima separating the inner and outer minima. The minima at large R are related to the centrifugal barriers on the long-range potential. The inner minima instead arise from the reduction of entropy that occurs as the chemical bonding between the $^1CH_2$ and the H_2 becomes significant.

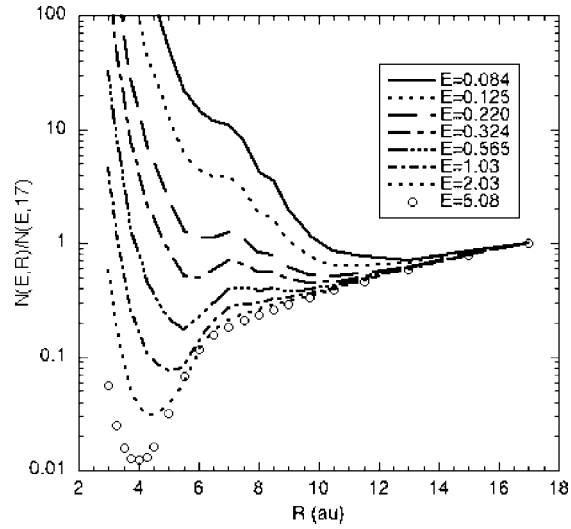

Figure 5. Plot of the microcanonical number of states $N(E,R)$ for motion on a given dividing surface vs the separation R. These fluxes, which are plotted for a range of energies E (in kcal mol^{-1}), are each normalized to their value at $R = 17$ Bohr. For $R > 8$ Bohr, the dividing surface corresponds to the center-of-mass separation. For $R < 8$ Bohr, the dividing surface corresponds to a fixed distance between the H_2 center of mass and the pivot points 1 Bohr above and below the C atom in the CH_2 plane.

Statistical assumptions for the crossing probabilities at each of these transition states yield an effective transition state number of states given by[47]

$$1/N_{\mathrm{eff}} = 1/N_{\mathrm{inner}} + 1/N_{\mathrm{outer}} - 1/N_{\mathrm{max}}$$

where N_{inner} and N_{outer} are the values for $N(R)$ at the inner and outer minima, while N_{max} is the value at the maxima. Assuming that N_{max} is large yields the expression

$$1/N_{\mathrm{eff}} = 1/N_{\mathrm{inner}} + 1/N_{\mathrm{outer}}$$

which provides a lower bound to the statistically based effective flux. Results are presented below for calculations that employ either the latter expression for N_{eff} or simply the minimum of N_{inner} and N_{outer}. These two results provide an indication of the range of values that might be expected for the high-pressure addition rate. A separation of 7 Bohr was used to separate the inner and outer transition state regions.

The present theoretical predictions for the $^1CH_2 + H_2$ high-pressure addition rate coefficient are illustrated in Figure 6. The effective two transition state prediction for this rate coefficient is well-reproduced over the 10−1500 K range by the expression $7.51 \times 10^{-9}\ T^{-0.762}\ \exp(-9.01/T) + 1.71 \times 10^{-12}\ T^{0.467}\ \exp(-2.26/T)$, where T is in K and the rate is in cm^3 molecule^{-1} s^{-1}. The outer transition state is seen to play a role in the kinetics only for temperatures of about 100 K and lower. As might be expected given the absence of a long-range minimum, the effective and minimum transition state results are fairly similar, differing by only 30% or less. The trajectory simulations on the CCSD(T)/aug-cc-pvtz analytic surface indicate that the dynamical correction factors to the effective transition state theory predictions are remarkably close to unity. In particular,

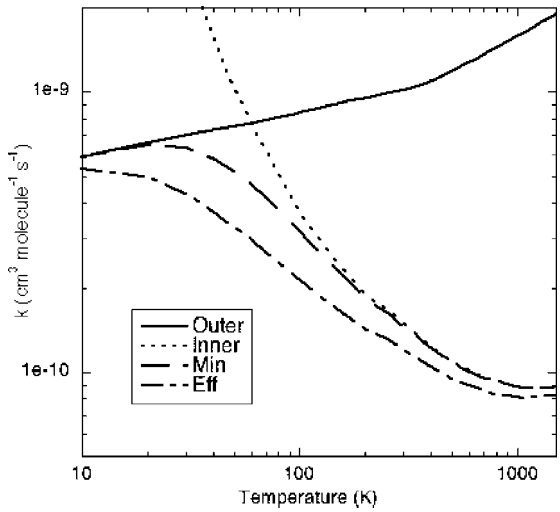

Figure 6. Plot of the theoretically predicted high-pressure rate coefficient for $^1CH_2 + H_2$. The solid and dotted lines denote predictions based on only the outer and inner transition states, respectively. The dashed line denotes the predictions obtained by taking the minimum of the inner and outer transition state fluxes. The dot−dash line denotes the predictions obtained for the effective transition state approximation discussed in the text.

TABLE 1: Bimolecular Rate Coefficients for the Removal of $^1CH_2$ with H_2 (k_1) and D_2 (k_2) Probing the $^PR_{1,J-1}$ Branch $J = 3$ (Ortho 3_{12}) Line over the Temperature Range 195−798 K Where the Errors Represent Statistical Uncertainty (2σ) in the Experimental Data

temperature (K)	$10^{-10} \times k_1$ (cm^3 molecules^{-1} s^{-1})	$10^{-11} \times k_2$ (cm^3 molecules^{-1} s^{-1})
195	1.030 ± 0.021	5.77 ± 0.27
298	1.094 ± 0.064	6.39 ± 0.47
398	1.054 ± 0.044	5.77 ± 0.36
498	1.072 ± 0.045	6.49 ± 0.52
598	1.087 ± 0.073	6.45 ± 0.44
698	1.024 ± 0.093	5.91 ± 0.22
798	1.098 ± 0.080	6.14 ± 0.35

values of 1.02, 0.99, 1.00, 0.99, and 0.94 are obtained for temperatures of 78, 106, 152, 206, and 315 K, respectively.

The rovibrational properties of the fragments are required for the low-pressure limit evaluations of the branching ratio and for the sample master equation evaluations of the pressure dependence. These properties were obtained from QCISD(T)/aug-cc-pvtz evaluations. The reaction exothermicity was obtained from QCISD(T)/CBS calculations. For the $^1CH_2 + H_2$ reaction, the zero K reaction exothermicity to produce $CH_3 + H$ is calculated to be 14.57 kcal mol^{-1}. For $^1CH_2 + D_2$, the $CH_2D + H$ and $CHD_2 + H$ product channels are predicted to be 14.37 and 16.00 kcal mol^{-1} exothermic, respectively.

The present CCSD(T), QCISD(T), CASPT2, and CAS + 1 + 2 + QC electronic structure calculations were all performed with the MOLPRO software package.[48] This package uses the Celani and Werner formulation of the CASPT2 approach.[49−51]

4. Results and Discussion

4.1. Kinetics of the Reaction $^1CH_2$ with H_2 and D_2 from 195 to 798 K. The kinetics of reactions 1 and 2 have been studied from 195 to 798 K and are summarized in Table 1 and Figure 7. The results at 195 K are independent of the nuclear state (ortho or para) of $^1CH_2$, flow rate (factor 3 variation), or laser power (factor 3 variation). As can be seen from the summary, the kinetics are essentially temperature-independent with $k_1 = (10.48 \pm 0.32) \times 10^{-11}$ cm^3 molecule^{-1} s^{-1} and $k_2 = (5.98 \pm 0.34) \times 10^{-11}$ cm^3 molecule^{-1} s^{-1}, where the errors represent 2σ, giving a ratio $k_1/k_2 = 1.75 \pm 0.11$.

The experimental results of this study are in good agreement with the work of Hancock and co-workers.[16,17] The lower temperature results of Wagener[15] lie outside the combined experimental uncertainties, and the higher precision results of this study do not reveal any negative temperature dependence. For condensable substrates, concentration measurements at low temperatures can be problematic; however, no such problems are expected for hydrogen and deuterium. Other recent work in this laboratory on $^1CH_2$ kinetics[24] has demonstrated temperature dependencies consistent with other work (positive for relaxation with inert gases[15,17] and negative for reactions with alkenes[52]); therefore, it seems unlikely that the lack of any observed experimental temperature dependence is due to a systematic error.

The observed isotope ratio, $k_1/k_2 = 1.75 \pm 0.11$, is significantly greater than the ratio of 1.33 that would be expected from mass effects on the long-range collisional rate alone. However, this is not the first time that large isotopic ratios have been observed for barrierless insertion reactions.[53] The reaction of CH with normal and deuterated methane has been studied in this laboratory[54] and by Thiesmann et al.[55] These reactions are believed to occur via the insertion of CH into a C−H(D) bond forming an energized ethyl radical, which subsequently decomposes to H + ethene, and the reactions have a slight negative temperature dependence. The mass effect on the ratio of rate coefficients k_{CH+CH_4}/k_{CH+CD_4} on deuterating the methane is small (1.05), but both groups report room temperature rate coefficient ratios of approximately 1.5. The theoretical calculations from Taatjes and Klippenstein[53] indicate that such large values are readily explained by changes in the vibrational frequencies and zero point energy at the transition state.

While at higher temperatures there is agreement in the magnitude of the rate coefficients, the disagreement between experiment and theory in the temperature dependence of the kinetics of reactions 1 and 2 warrants further investigation, particularly at low temperatures where the disagreement is most pronounced. The recent construction and commissioning of a pulsed Laval system at Leeds offers the possibility to study kinetics (and possibly product branching ratios) down to ~50 K.[56]

4.2. Branching Ratios. In any branching ratio study, there is the possibility that the observed product may not arise from the target reaction. The fact that H atom production is temporally correlated with $^1CH_2$ minimizes the possibility for this particular study.

4.2.1. H Atom Yield from $^1CH_2 + H_2$. The H atom yield as a function of temperature from reaction 1 is summarized in the second column of Table 2. The yields at 298, 398, and 500 K are taken from our previous study.[19] The value at 195 K, measured as part of this work, continues the observed trend with the fraction of electronic deactivation increasing with decreasing temperature.

For the inert gases, the cross-section for deactivation has previously been correlated with the well depth of the interactive potential in a Parmenter−Seaver plot[57] by Ashfold et al.[13] Figure 8 shows the plot for data recently obtained in this laboratory,[24] highlighting the strong correlation between these parameters. The plot also shows the deactivation cross-section for H_2 (15% of the total removal cross-section). The point for H_2 (and D_2) lies some way off this line. Additionally, the results of our kinetic and branching ratio studies indicate that the efficiency

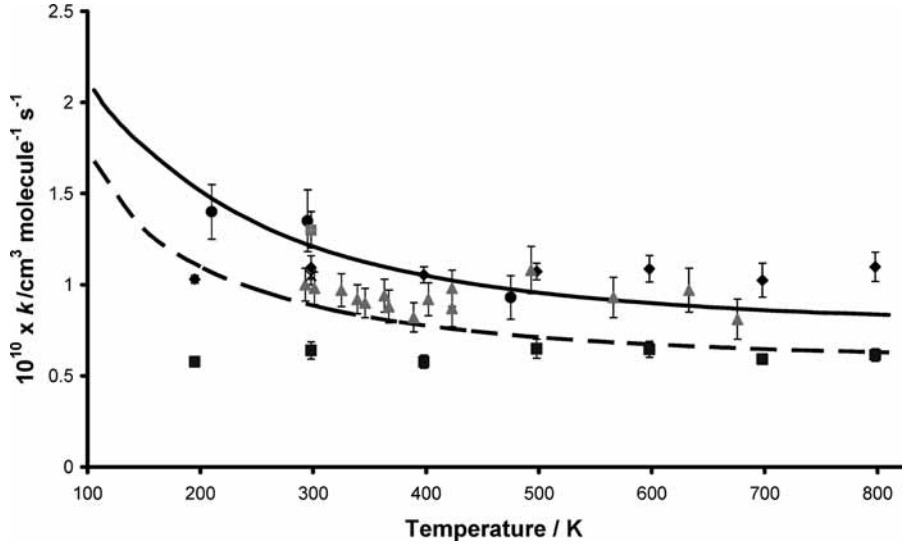

Figure 7. Temperature dependence of the rate coefficients for the removal of $^1CH_2$ with H_2 and D_2. Black diamond, k_1, this work; black square, k_2, this work; gray triangle, k_1, Hancock and Heal;[17] black circle, Wagener;[15] gray square, Ashfold et al.;[13] and ×, Langford et al.[14] The solid and dashed lines are the theoretical calculations for $^1CH_2$ with H_2 and D_2, respectively.

TABLE 2: Absolute Yield of H and (H + D) from the Reactions of $^1CH_2 + H_2$ and D_2, Respectively, as a Function of Temperature Where the Reported Errors Describe the Statistical (2σ) Uncertainty in the Experimental Data

	$^1CH_2 + H_2$	$^1CH_2 + D_2$				
T/K	α_H	α_H	α_D	$\alpha_H + \alpha_D$	H:D expt	H:D theory
195	0.71 ± 0.07	0.49 ± 0.07	0.24 ± 0.09	0.73 ± 0.12	2.0 ± 0.8	1.36
298	0.85± 0.08	0.47 ± 0.05	0.28 ± 0.09	0.75 ± 0.10	1.7 ± 0.6	1.34
398	0.92 ± 0.08	0.55 ± 0.07	0.34 ± 0.04	0.89 ± 0.10	1.6 ± 0.4	1.31
500	1.01 ± 0.10					

of the deactivation decreases with temperature in contrast to the inert gases where quenching has a weak ($T^{0.4-1.2}$) but positive temperature dependence.

The temperature dependence of k_{1a} indicates that the mechanism of deactivation by H_2 is different from the intersystem crossing induced by collisions with inert gases. $^3CH_2$ reacts with H_2, but with a large activation energy, so that the triplet $CH_2 + H_2$ surface is repulsive and may cross the attractive singlet surface. Depending on the location of this crossing, it could provide a mechanism for transfer from the singlet to the triplet surface. In such circumstances, the overall rate coefficient, k_1, would correspond to the capture rate coefficient with k_{1a}/k_{1b} increasing as the temperature falls. A more detailed discussion of the mechanism is beyond the scope of this paper.

4.2.2. H and D Atom Yields from $^1CH_2 + D_2$. Figure 9 shows a typical experimental plot for the study of the H and D atom yields from $^1CH_2 + D_2$. H (circles) and D (triangles) atom signals were recorded in back-to-back experiments with the probe laser being tuned back and forth between H and D wavelengths. Subsequently, D_2 was replaced with H_2, and the experiment was repeated, monitoring the H atom signal with identical initial $^1CH_2$ concentrations (squares). The data have been normalized to the previously determined yield of 0.85 for

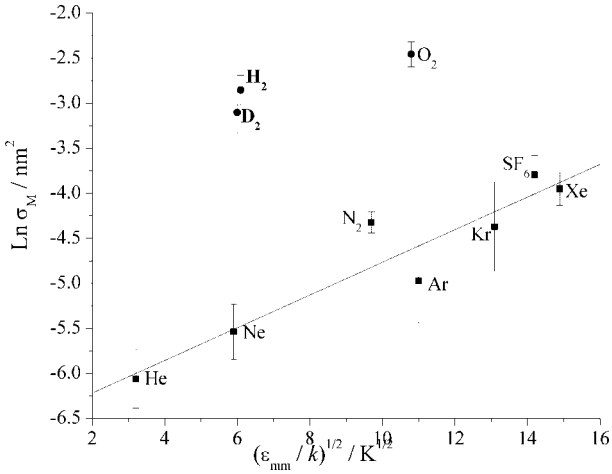

Figure 8. Plot of the logarithm of the experimentally determined cross-sections for quenching of CH_2 ($^1A_1$), $\ln\sigma_M$ vs the well depth values $(\epsilon_{MM}/k)^{1/2}$, where the straight lines are least-squares fits to the experimental data points, and the errors represent the statistical uncertainty (2σ) in the experimental data.

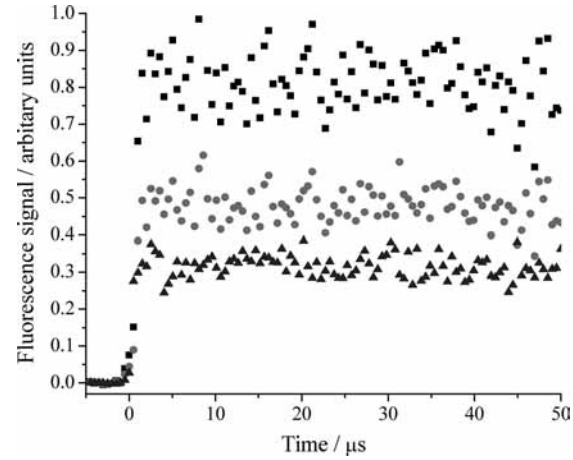

Figure 9. Absolute H atom signal from $^1CH_2 + H_2$ (black square), H atom signal from $^1CH_2 + D_2$ (gray circle), and D atom signal from $^1CH_2 + D_2$ (black triangle) at 295 K.

the H atom yield for $^1CH_2 + H_2$. The experimental and theoretical yield data from reaction 2 are summarized in the last five columns of Table 2.

Within experimental error, the combined yield of H and D atom from $^1CH_2 + D_2$ is identical to the H atom yield from $^1CH_2 + H_2$, suggesting that, as might be expected, the atom yield is independent of isotopic substitution. Atom yields are dominated by H atom elimination. This is expected on a statistical basis as the channel leading to $CH_2D + D$ has a higher zero point energy and a lower number of states in the transition state in comparison to the $CHD_2 + H$ channel. The experimental and theoretical H:D ratios from reaction 2 are compared in the last two columns of Table 2. Within experimental errors, the H:D ratios from experiment and theory are in satisfactory agreement, and the experimental results are therefore consistent with the expected randomization of energy in the relatively long-lived CH_2D_2 intermediate. The propensity for H atom elimination from energized methane was exploited in earlier studies of methyl radicals with D atoms.[58,59] Once corrections had been made for isotopic effects, RRKM-based calculations of the H and D atom elimination channels from CH_xD_{4-x} allowed for an estimation of the high pressure rate coefficient for $CH_3 + H$.

Early work on the product yields of reactions 1 and 2 was dependent on end product analysis of the stable products. Studies by Bell and Kistiakowsky[60] showed experimentally that the reaction proceeded via insertion rather than abstraction, and this study confirms directly that abstraction is not the dominant process (abstraction in reaction 2 would lead to 100% D); the experimental and theoretical results in this work show that the reactive products are consistent with an insertion mechanism.

4.3. Implications for Models of Outer Planetary Atmospheres. In models of the atmospheres of the outer planets such as Jupiter and Neptune, the primary source and fate of methylene radicals involve the following processes.[61,62]

$$CH_4 \xrightarrow{h\nu} {}^1CH_2 + H_2$$

$$^1CH_2 + H_2 \rightarrow CH_3 + H$$

The temperature of Jupiter's stratosphere is approximately 200 K; at 1 mbar,[62,63] the results presented show that around 30% of collisions between $^1CH_2$ and H_2 would result in deactivation and not reaction. The formation of $^3CH_2$ is included in the models, with a ratio of k_{1a}:k_{1b} of 1.0:7.5, derived from the studies of Langford et al.[14] and Braun et al.[20] This is clearly an underestimation of the rate of collisional deactivation, and a ratio of approximately 1:2 appears more appropriate at 200 K given the results presented. Ensuring an accurate determination of such a branching ratio is not only important in terms of generating the correct methyl radical abundance but ultimately has implications for the build up of several more complex species. The rate coefficient for the reaction of $^3CH_2$ with H_2 is very low; hence, $^3CH_2$ radicals will be available to undergo reactions that build more complex hydrocarbons, for example, the reaction of $CH_3 + {}^3CH_2$ is thought to be the mechanism for C_2H_4 formation.[3] The reaction of H atoms, generated from $^1CH_2 + H_2$ among other reactions, with $^3CH_2$ is included as a mechanism for CH radical and H_2 formation. The reactivity of CH is such that it is involved in a wide range of complex reactions relevant for the formation of more complex species.[64]

Acknowledgment. We acknowledge the support of EPSRC for a studentship for K.L.G. and for a grant (GR/T28560/01) under which this work was performed. The work at Argonne was supported by the Division of Chemical Sciences, Geosciences, and Biosciences, the Office of Basic Energy Sciences, the U.S. Department of Energy, under Contract DE-AC02-06CH11357.

References and Notes

(1) Miller, J. A.; Melius, C. F. *Combust. Flame* **1992**, *91*, 21.
(2) Westmoreland, P. R.; Dean, A. M.; Howard, J. B.; Longwell, J. P. *J. Phys. Chem.* **1989**, *93*, 8171.
(3) Gladstone, G. R.; Allen, M.; Yung, Y. L. *Icarus* **1996**, *119*, 1.
(4) Smith, G. P.; Nash, D. *Icarus* **2006**, *182*, 181.
(5) Moses, J. I.; Fouchet, T.; Bezard, B.; Gladstone, G. R.; Lellouch, E.; Feuchtgruber, H. *J. Geophys. Res.-[Planets]* **2005**, 110.
(6) Bezard, B.; Romani, P. N.; Feuchtgruber, H.; Encrenaz, T. *Astrophys. J.* **1999**, *515*, 868.
(7) Leung, K. M.; Lindstedt, R. P. *Combust. Flame* **1995**, *102*, 129.
(8) Blitz, M. A.; Beasley, M. S.; Pilling, M. J.; Robertson, S. H. *Phys. Chem. Chem. Phys.* **2000**, *2*, 805.
(9) Georgievskii, Y.; Miller, J. A.; Klippenstein, S. J. *Phys. Chem. Chem. Phys.* **2007**, *9*, 4259.
(10) Bley, U.; Temps, F. *J. Chem. Phys.* **1993**, *98*, 1058.
(11) Jensen, P.; Bunker, P. R. *J. Chem. Phys.* **1988**, *89*, 1327.
(12) Bauschlicher, C. W.; Haber, K.; Schaefer, H. F.; Bender, C. F. *J. Am. Chem. Soc.* **1977**, *99*, 3610.
(13) Ashfold, M. N. R.; Fullstone, M. A.; Hancock, G.; Ketley, G. W. *Chem. Phys.* **1981**, *55*, 245.
(14) Langford, A. O.; Petek, H.; Moore, C. B. *J. Chem. Phys.* **1983**, *78*, 6650.
(15) Wagener, R. *Z. Naturforsch., A: Phys. Sci.* **1990**, *45a*, 649.
(16) Biggs, P.; Hancock, G.; Heal, M. R.; McGarvey, D. J.; Parr, A. D. *Chem. Phys. Lett.* **1991**, *180*, 533.
(17) Hancock, G.; Heal, M. R. *J. Phys. Chem.* **1992**, *96*, 10316.
(18) Georgievskii, Y.; Klippenstein, S. J. *J. Chem. Phys.* **2005**, 122.
(19) Blitz, M. A.; Choi, N.; Kovacs, T.; Seakins, P. W.; Pilling, M. J. *Proc. Combust. Inst.* **2005**, *30*, 927.
(20) Braun, W.; Bass, A. M.; Pilling, M. *J. Chem. Phys.* **1970**, *52*, 5131.
(21) Robertson, S. H.; Seakins, P. W. *Phys. Chem. Chem. Phys.* **2007**, *9*, 4053.
(22) Choi, N.; Blitz, M. A.; McKee, K.; Pilling, M. J.; Seakins, P. W. *Chem. Phys. Lett.* **2004**, *384*, 68.
(23) Gannon, K. L.; Glowacki, D. R.; Blitz, M. A.; Hughes, K. J.; Pilling, M. J.; Seakins, P. W. *J. Phys. Chem. A* **2007**, *111*, 6679.
(24) Gannon, K. L. Kinetics and product studies of reactions relevant to the atmospheres of the outer planets. Ph.D. Thesis, University of Leeds, 2007.
(25) Fisher, G. J.; Maclean, A. F.; Schnizer, A. W. *J. Org. Chem.* **1953**, *18*, 1055.
(26) Arendale, W. F.; Fletcher, W. H. *J. Chem. Phys.* **1957**, *26*, 793.
(27) Morgan, C. G.; Drabbels, M.; Wodtke, A. M. *J. Chem. Phys.* **1996**, *104*, 7460.
(28) Wade, E. A.; Clauberg, H.; Kim, S. K.; Mellinger, A.; Moore, C. B. *J. Phys. Chem. A* **1997**, *101*, 732.
(29) Fikri, M.; Meyer, S.; Roggenbuck, J.; Temps, F. *Faraday Discuss.* **2001**, *119*, 223.
(30) Kollmar, H.; Staemmler, V. *Theor. Chim. Acta* **1979**, *51*, 207.
(31) Pepper, M. J. M.; Shavitt, I.; Schleyer, P. V.; Glukhovtsev, M. N.; Janoschek, R.; Quack, M. *J. Comput. Chem.* **1995**, *16*, 207.
(32) Jursic, B. S. *J. Mol. Struct. (THEOCHEM)* **1999**, *467*, 103.
(33) Harding, L. B.; Georgievskii, Y.; Klippenstein, S. J. *J. Phys. Chem. A* **2005**, *109*, 4646.
(34) Klippenstein, S. J.; Georgievskii, Y.; Harding, L. B. *Phys. Chem. Chem. Phys.* **2006**, *8*, 1133.
(35) Klippenstein, S. J.; East, A. L. L.; Allen, W. D. *J. Chem. Phys.* **1996**, *105*, 118.
(36) Langhoff, S. R.; Davidson, E. R. *Int. J. Quantum Chem.* **1974**, *8*, 61.
(37) Davidson, E. R.; Silver, D. W. *Chem. Phys. Lett.* **1977**, *52*, 403.
(38) Klippenstein, S. J.; Georgievskii, Y.; Harding, L. B. *Proc. Combust. Inst.* **2002**, *29*, 1229.
(39) Dunning, T. H. *J. Chem. Phys.* **1989**, *90*, 1007.
(40) Kendall, R. A.; Dunning, T. H.; Harrison, R. J. *J. Chem. Phys.* **1992**, *96*, 6796.
(41) Raghavachari, K.; Trucks, G. W.; Pople, J. A.; Headgordon, M. *Chem. Phys. Lett.* **1989**, *157*, 479.
(42) Pople, J. A.; Headgordon, M.; Raghavachari, K. *J. Chem. Phys.* **1987**, *87*, 5968.
(43) Andersson, K.; Malmqvist, P. A.; Roos, B. O.; Sadlej, A. J.; Wolinski, K. *J. Phys. Chem.* **1990**, *94*, 5483.
(44) Andersson, K.; Malmqvist, P. A.; Roos, B. O. *J. Chem. Phys.* **1992**, *96*, 1218.

(45) Martin, J. M. L.; Uzan, O. *Chem. Phys. Lett.* **1998**, *282*, 16.
(46) Zhang, X.; Zou, L.; Harding, L. B.; Bowman, J. M. *J. Phys. Chem. A* **2004**, *108*, 8980.
(47) Klippenstein, S. J.; Khundkar, L. R.; Zewail, A. H.; Marcus, R. A. *J. Chem. Phys.* **1988**, *89*, 4761.
(48) Werner, H.-J.; Knowles, P. J.; Almlof, J.; Amos, R. D.; Berning, A.; Cooper, D. L.; Deegan, M. J. O.; Dobbyn, A. J.; Eckert, F.; Elbert, S. T.; Hampel, C.; Lindh, R.; Lloyd, A. W.; Meyer, W.; Nicklass, A.; Peterson, K.; Pitzer, R.; Stone, A. J.; Taylor, P. R.; Mura, M. E.; Pulay, P.; Schutz, M.; Stoll, H.; Thorsteinsson, T. MOLPRO, 2006.1 ed.; MOLPRO: Cardiff, U.K., 2006.
(49) Werner, H. J. *Mol. Phys.* **1996**, *89*, 645.
(50) Celani, P.; Werner, H. J. *J. Chem. Phys.* **2000**, *112*, 5546.
(51) Celani, P.; Werner, H. J. *J. Chem. Phys.* **2003**, *119*, 5044.
(52) Hayes, F.; Lawrance, W. D.; Staker, W. S.; King, K. D. *J. Phys. Chem.* **1996**, *100*, 11314.
(53) Taatjes, C. A.; Klippenstein, S. J. *J. Phys. Chem. A* **2001**, *105*, 8567.
(54) Blitz, M. A.; Johnson, D. G.; Pesa, M.; Pilling, M. J.; Robertson, S. H.; Seakins, P. W. *J. Chem. Soc. Faraday Trans.* **1997**, *93*, 1473.
(55) Thiesemann, H.; MacNamara, J.; Taatjes, C. A. *J. Phys. Chem. A* **1997**, *101*, 1881.
(56) Taylor, S. E.; Goddard, A.; Blitz, M. A.; Cleary, P. A.; Heard, D. E. *Phys. Chem. Chem. Phys.* **2008**, *10*, 422.
(57) Lin, H. M.; Seaver, M.; Tang, K. Y.; Knight, A. E. W.; Parmenter, C. S. *J. Chem. Phys.* **1979**, *70*, 5442.
(58) Seakins, P. W.; Robertson, S. H.; Pilling, M. J.; Wardlaw, D. M.; Nesbitt, F. L.; Thorn, R. P.; Payne, W. A.; Stief, L. J. *J. Phys. Chem.* **1997**, *101*, 9974.
(59) Su, M. C.; Michael, J. V. *Proc. Combust. Inst.* **2002**, *29*, 1219.
(60) Bell, J. A.; Kistiakowsky, G. B. *J. Am. Chem. Soc.* **1962**, *84*, 3417.
(61) Monks, P. S.; Romani, P. N.; Nesbitt, F. L.; Scanlon, M.; Stief, L. J. *J. Geophys. Res.* **1993**, *98*, 17115.
(62) Randall Gladstone, G.; Allen, M.; Yung, Y. L. *Icarus* **1996**, *119*, 1.
(63) Laufer, A. H.; Gardner, E. P.; Kwok, T. L.; Yung, Y. L. *Icarus* **1983**, *56*, 560.
(64) Seakins, P. W. Annu. Rep. Prog. Chem., Sect. C: Phys. Chem. 2007, *103*, 173.

JP803038S